Improvements to ultrasonic beamformer design and implementation derived from the task-based analytical framework

Nghia Q. Nguyen and , Richard W. Prager, and Michael F. Insana

Citation: The Journal of the Acoustical Society of America **141**, 4427 (2017); doi: 10.1121/1.4985187
View online: http://dx.doi.org/10.1121/1.4985187
View Table of Contents: http://asa.scitation.org/toc/jas/141/6
Published by the Acoustical Society of America

Improvements to ultrasonic beamformer design and implementation derived from the task-based analytical framework

Nghia Q. Nguyen[a] and Richard W. Prager
Department of Engineering, University of Cambridge, Cambridge CB2 1PZ, United Kingdom

Michael F. Insana
Department of Bioengineering and Beckman Institute, University of Illinois at Urbana-Champaign, Urbana, Illinois 61801, USA

(Received 2 November 2016; revised 5 April 2017; accepted 23 May 2017; published online 15 June 2017)

The task-based framework, previously developed for beamformer comparison [Nguyen, Prager, and Insana, J. Acoust. Soc. Am. **140**, 1048–1059 (2016)], is extended to design a new beamformer with potential applications in breast cancer diagnosis. The beamformer is based on a better approximation of the Bayesian strategy. It is a combination of the Wiener-filtered beamformer and an iterative process that adapts the generated image to specific features of the object. Through numerical studies, the new method is shown to outperform other beamformers drawn from the framework, but at an increase in computational cost. It requires a preprocessing step where the scattering field is segmented into regions with distinct statistical properties. Segmentation errors become a major limitation to the beamformer performance. All the beamformers under investigation are tested using data obtained from an instrumented ultrasound machine. They are implemented using a new time delay calculation, recently developed in the pixel-based beamforming studies presented here, which helps to overcome the challenge posed by the shift-variant nature of the imaging system. The efficacy of each beamformer is evaluated based on the quality of generated images in the context of the task-based framework. The *in vitro* results confirm the conclusions drawn from the simulations.
 [http://dx.doi.org/10.1121/1.4985187]

[KTW] Pages: 4427–4437

I. INTRODUCTION

A task-based approach has been used to evaluate and optimize medical imaging systems,[1] including ultrasound imaging.[2,3] In the approach, systems perform *diagnostic tasks* by transporting information from the objects being examined to the observers who make decisions. The framework exploits the *Bayesian ideal observer*—simply known as the ideal observer (IO)—to analyze the image formation process. This combines all relevant information, including prior knowledge of the scanned object, the system model, and statistical properties of the data, to make the best possible decision for a given task. The ideal observer, therefore, provides the upper bound for diagnostic performance of the imaging instrument. It is usually used in theoretical analysis or simulation, where a model of visual detection is available, to identify promising approaches that are worth investigating in clinical studies.

The IO was first applied to ultrasound imaging for detecting small, low-contrast lesions in breast cancer diagnosis by Smith, Wagner, and their colleagues.[4,5] It was shown how properties of the transducer and features of the object influence the speckle and thus the ability of the instrument to detect the lesion. As a result, the ideal performance can be quantified and related to the number of speckles found inside the lesion. However, non-linear processes, such as demodulation and amplitude compression, are involved in the generation of B-mode ultrasound images. It is therefore difficult to obtain a stochastic model that directly relates the backscattered sound field to the pixels in the B-mode image. For the IO test statistic to be calculated, Smith and Wagner adopted several significant assumptions. First, speckle spots rather than pixels were used to determine the statistical properties of the data. The framework was also confined to the focal zone where speckle spots are most independent. The system was assumed to be linear shift-invariant without noise and only low-contrast lesions were considered. Despite these limitations, the analysis provided design criteria that guided subsequent work in speckle reduction,[6] beamformation,[7] post-processing,[8] and transducer selection.[9]

Modern ultrasound instruments have an ability to digitize and store all echo data received at individual transducer elements.[10] This allows us to develop an alternative framework in the radio-frequency (RF) domain, where the echoes can be modeled as a linear transformation of the scattering object.[11] It simplifies the complexity of the joint probability distributions on the image pixels and relaxes some of the limiting assumptions involved in the IO development. Such an analysis becomes increasingly relevant as ultrasound high-end products have greater flexibility to change their

[a]Electronic mail: nqn20@cam.ac.uk

configuration for data processing so as to provide patient-specific performance.

In the first part of the study,[12] hereafter referred as Paper I, we developed an IO analysis applied to pre-summed RF data for beamformer comparisons. Through a combination of power series expansion[13] and the matrix inversion lemma,[14] we showed how two popular beamformers, Minimum Variance (MV) and Wiener-filtered (WF), could be viewed in a task-based framework as approximations to the ideal strategy. These beamformers were compared to each other by analyzing the conditions when each approximation holds. They were evaluated numerically on a panel of five tasks related to key features of a breast lesion in cancer diagnosis. Both analytical and numerical results show that the WF outperforms the MV, especially in low echo signal-to-noise ratio (SNR) conditions. The results also showed the substantial improvement of the WF over the standard delay-and-sum (DS) beamformer. In the task involving discriminating high-contrast features, however, the improvement was least. This was explained by the fact that the approximations, used to derive both MV and WF, were based on low-contrast features of the object. Hence these beamformers become less effective when applied to tasks that have relevant information encapsulated in high-contrast features.

In this paper, we present a beamformer that is designed to reconstruct valid images for a wider range of tasks that includes those with large signal heterogeneities. It is derived from an approximation of the IO that relaxes the low-contrast assumption for the object.[15] Similar to the WF and MV, we develop the new beamformer under the linear-shift-invariant (LSI) assumption for the imaging system. We also assume that the pulse-echo impulse-responses and noise power are known. As in Paper I, the resulting beamformer is numerically evaluated on the same panel of five tasks related to breast sonography. We then implement the beamformers on data acquired from an ultrasound system by imaging a tissue-mimicking phantom. The implementations face a challenge posed by the shift-variant nature of the real ultrasound imaging system. We show how this issue can be resolved by combining each of the beamformers with a new time delay calculation, recently developed in our pixel-based beamforming studies.[16,17]

The remainder of the paper is organized as follows. Section II summarizes the main components of the IO analysis. We then present the first-order approximation that is still accurate with high-contrast features from which the new beamformer is drawn. This beamformer, along with the WF and MV derived in Paper I, is evaluated using Monte-Carlo studies in Sec. III. The beamformers are then applied to data generated under more realistic conditions, including the shift-variant data, in Sec. IV. The results are discussed in Sec. V with some concluding remarks in Sec. VI.

II. METHODS

We first summarize the background that leads to the IO analysis, including the two approximations of the IO test statistic for deriving the MV and WF beamformers. Details are provided in Paper I. We then show how the IO framework can be extended to form a new ultrasound beamformer.

A. Signal modeling

By assuming the ultrasound imaging system is linear, we can model the two-dimensional (2-D) RF data frame at each receive channel as a noisy linear transformation of the scattering object in the spatial domain. Stacking them together, we form an expression to generate pre-summed RF data $\mathbf{g}$ for one imaging frame as

$$\mathbf{g} = \mathbf{H}\mathbf{f} + \mathbf{n}, \tag{1}$$

where $\mathbf{H}$ is the overall system matrix, $\mathbf{f}$ is a vector of the scattering object, and $\mathbf{n}$ is the Gaussian noise with variance σ_n^2, $\mathbf{n} \sim \mathcal{N}(0, \sigma_n^2\mathbf{I})$. By further assuming the system is linear-shift-invariant (LSI), matrix $\mathbf{H}$ is a cascade of block-Toeplitz matrices that characterize the data generation at receive channels. In our study, we approximate these as the corresponding circulant matrices to facilitate fast matrix-vector product computations.[18]

The beamformer applied to pre-summed RF data $\mathbf{g}$ is a filtering and summation process, characterized by matrix $\mathbf{B}$. The beamformed data are given by $\mathbf{g}_B = \mathbf{B}^t\mathbf{g}$. The B-mode image $\mathbf{b}$ is generated through demodulation, $\mathbf{b} = \mathcal{O}\mathbf{g}_B$. Our goal is to find a beamformer $\mathbf{B}$ that maximizes the task information transferred from channel data to the B-mode image. In the task-based analysis, the information is measured through the performance of the ideal observer.[2,3]

B. Ideal observer

The development of the IO is based on modeling the scattering object $\mathbf{f}$ as a zero-mean multivariate-normal (MVN) process, $\mathbf{f} \sim \mathrm{MVN}(0, \mathbf{\Sigma}_{obj})$. The covariance matrix is given by $\mathbf{\Sigma}_{obj} = \sigma_{obj}^2(\mathbf{I} + \mathbf{S}_i)$. It contains a component $\mathbf{S}_i$ that carries the benign or malignant feature underlying the ith class ($i = 0$ indicating benign and $i = 1$ for malignant). Task contrast is defined as the difference between the two $\mathbf{S}_i$, i.e., $\Delta\mathbf{S} = \mathbf{S}_1 - \mathbf{S}_0$.

By passing the scattering object vector $\mathbf{f}$ through the linear transformation of Eq. (1), we obtain the RF data vector $\mathbf{g}$ which is also MVN distributed, $\mathbf{g} \sim \mathrm{MVN}(0, \mathbf{\Sigma}_i)$. Covariance matrix $\mathbf{\Sigma}_i$, however, is a non-diagonal matrix because of the correlations among samples introduced by $\mathbf{H}$. It is given as

$$\mathbf{\Sigma}_i = \sigma_{obj}^2\mathbf{H}(\mathbf{I} + \mathbf{S}_i)\mathbf{H}^t + \sigma_n^2\mathbf{I}. \tag{2}$$

The test statistic of the IO acting on $\mathbf{g}$ is defined through the log-likelihood ratio

$$\lambda(\mathbf{g}) \triangleq \ln\left(\frac{p_1(\mathbf{g})}{p_0(\mathbf{g})}\right) \simeq \frac{1}{2}\mathbf{g}^t\left(\mathbf{\Sigma}_0^{-1} - \mathbf{\Sigma}_1^{-1}\right)\mathbf{g}, \tag{3}$$

where the second expression is obtained by eliminating terms unrelated to data $\mathbf{g}$. A larger value for this scalar variable indicates a greater likelihood for condition 1 than

condition 0. The IO that adopts this strategy uses the data to gain the maximal performance in the sense that it achieves the greatest area under the receiver operating characteristic (ROC) curve for each of the discrimination tasks.

Although the IO test statistic is well defined, its calculation is not straightforward because of the need to invert both of the Σ_i. In Paper I, we showed how this calculation can be accomplished by using power-series expansions. Hence, the IO performance can be measured numerically using two-alternative forced choice (2AFC) methods.[18] The area under the ROC (area under curve: AUC) is measured as follows. We generate a large number of pairs of RF data $\mathbf{g}$, and calculate $\lambda_i = \lambda(\mathbf{g}|i)$ for each pair of $\mathbf{g}$'s generated for each class $i=0$ and $i=1$. At each pair, we set a response o equal to 1 if $\lambda_1 > \lambda_0$ and equal to 0 otherwise. By taking the average all of the responses, the AUC can be estimated based on the proportion of correct P_c, i.e., $P_c = \Pr(\lambda_1 > \lambda_0) = \text{AUC}$.

C. Beamforming derivations

The IO combines echo data from individual channels to make the best decision for each task, thus, optimal beamforming strategies are hidden in the closed-form expression of the test statistic. Through the matrix inversion lemma, we explore the IO test statistic and show how the MV and WF beamformers emerge as approximations of this strategy. Details of the derivations are provided in Paper I (Secs. III C and III D). The first approximation, used to derive the MV beamformer, is given by

$$\lambda(\mathbf{g}) \simeq \frac{1}{2}\mathbf{g}^t\mathbf{B}_{MV}\Delta\mathbf{S}\,\mathbf{B}_{MV}^t\mathbf{g}, \tag{4}$$

where

$$\mathbf{B}_{MV}^t = (\sigma_{obj}\mathbf{H}^t\boldsymbol{\Sigma}_n^{-1}\mathbf{H})^{-1}\mathbf{H}^t\boldsymbol{\Sigma}_n^{-1}\,. \tag{5}$$

Since $\mathbf{g}^t\mathbf{B}_{MV} = (\mathbf{B}_{MV}^t\mathbf{g})^t$, Eq. (4) suggests that the ideal performance can be achieved by matching the MV beamformed data $\mathbf{B}_{MV}^t\mathbf{g}$ squared with the task difference $\Delta\mathbf{S}$. Thus, the MV beamformer captures some important components of the IO and can filter out other information that is irrelevant to the task. It indicates the MV beamforming should be applied to the RF data $\mathbf{g}$.

The WF beamformer is derived using a second approximation given by

$$\lambda(\mathbf{g}) \simeq \frac{1}{2}\mathbf{g}^t\mathbf{B}_{WF}\Delta\mathbf{S}\,\mathbf{B}_{WF}^t\mathbf{g}, \tag{6}$$

where

$$\mathbf{B}_{WF}^t = \sigma_{obj}\Omega_s^{-1}\mathbf{H}^t \quad \text{and}$$
$$\Omega_s \triangleq \sigma_{obj}^2\mathbf{H}^t\mathbf{H} + \sigma_n^2\mathbf{I}\,. \tag{7}$$

The term $\sigma_{obj}\Omega_s^{-1}\mathbf{H}^t\mathbf{g}$ is recognized as a Wiener-filtered beamformer applied to the data $\mathbf{g}$. Similar to (4), Eq. (6) suggests the application of the WF beamformer to $\mathbf{g}$.

For the approximations to be accurate, both require $\mathbf{S}_i \simeq \mathbf{0}$ which happens in low-contrast tasks. Consequently, the beamformers may become less effective when they are applied to a task with high-contrast features. In Sec. II D, we develop an approximation that relaxes this requirement from which we derive a new ultrasonic beamformer.

D. Iterative Wiener beamformer

We start from Eq. (16) in Paper I in which we use the matrix inversion lemma to convert the test statistic in (3) into

$$\lambda(\mathbf{g}) = \frac{\sigma_{obj}^2}{2}\mathbf{g}^t\boldsymbol{\Sigma}_n^{-1}\mathbf{H}\mathbf{K}_n^{-1}\left(\boldsymbol{\Phi}_0^{-1} - \boldsymbol{\Phi}_1^{-1}\right)\mathbf{K}_n^{-1}\mathbf{H}^t\boldsymbol{\Sigma}_n^{-1}\mathbf{g}, \tag{8}$$

where $\boldsymbol{\Phi}_i \triangleq \mathbf{I} + (\mathbf{K}_n^{-1} + \mathbf{S}_i)$ and $\mathbf{K}_n \triangleq \sigma_{obj}^2\mathbf{H}^t\boldsymbol{\Sigma}_n^{-1}\mathbf{H}$.

For the power series expansion to be applied, we separate $\boldsymbol{\Phi}_{1,0}$ into *sum* and *difference* components of both data classes, given by

$$\boldsymbol{\Phi}_a = \mathbf{I} + \mathbf{K}_n^{-1} + \frac{1}{2}(\mathbf{S}_1 + \mathbf{S}_0) = \mathbf{I} + \mathbf{K}_n^{-1} + \mathbf{S}_a$$
$$\text{and } \Delta\boldsymbol{\Phi} = 0.5(\mathbf{S}_1 - \mathbf{S}_0) = 0.5\Delta\mathbf{S}, \tag{9}$$

where $\mathbf{S}_a = 0.5(\mathbf{S}_1 + \mathbf{S}_0)$. The covariance matrices are divided into $\boldsymbol{\Phi}_{1,0} = \boldsymbol{\Phi}_a \pm \Delta\boldsymbol{\Phi}$, from which we can decompose the matrix inversions into

$$\boldsymbol{\Phi}_{1,0}^{-1} = \boldsymbol{\Phi}_a^{-1/2}(\mathbf{I} \pm \boldsymbol{\Phi}_a^{-1/2}\Delta\boldsymbol{\Phi}\boldsymbol{\Phi}_a^{-1/2})^{-1}\boldsymbol{\Phi}_a^{-1/2}\,. \tag{10}$$

Applying the power series to the terms in parentheses and truncating at the first term, we obtain

$$\boldsymbol{\Phi}_1^{-1} \simeq \boldsymbol{\Phi}_a^{-1} - \boldsymbol{\Phi}_a^{-1}\Delta\boldsymbol{\Phi}\boldsymbol{\Phi}_a^{-1},$$
$$\boldsymbol{\Phi}_0^{-1} \simeq \boldsymbol{\Phi}_a^{-1} + \boldsymbol{\Phi}_a^{-1}\Delta\boldsymbol{\Phi}\boldsymbol{\Phi}_a^{-1}. \tag{11}$$

For the approximations in (11) to be accurate, we only need $\Delta\boldsymbol{\Phi}$, or $\Delta\mathbf{S}$, to be small while the feature contrast $\mathbf{S}_i$ still can be high. By substituting them into (8), we have

$$\lambda(\mathbf{g}) \simeq \frac{\sigma_{obj}^2}{2}\mathbf{g}^t\boldsymbol{\Sigma}_n^{-1}\mathbf{H}\mathbf{K}_n^{-1}\boldsymbol{\Phi}_a^{-1}\Delta\mathbf{S}\Phi_a^{-1}\mathbf{K}_n^{-1}\mathbf{H}^t\boldsymbol{\Sigma}_n^{-1}\mathbf{g}$$
$$= \frac{\sigma_{obj}^2}{2}\mathbf{g}^t\mathbf{H}\Omega_a^{-1}\Delta\mathbf{S}\Omega_a^{-1}\mathbf{H}^t\mathbf{g}, \tag{12}$$

where $\Omega_a \triangleq \Omega_s + \sigma_{obj}^2\mathbf{H}^t\mathbf{H}\mathbf{S}_a$.

Similar to the derivations of the MV and WF, (12) suggests that the beamformer $\Omega_a^{-1}\mathbf{H}^t$ should be applied to data $\mathbf{g}$. To see how $\Omega_a^{-1}\mathbf{H}^t\mathbf{g}$ is close to $\mathbf{f}$, we perform a similar derivation for the case of a perfect imaging system (i.e., $\mathbf{g} \sim \mathbf{f}$ with no noise and no blurring), and obtain the approximation:

$$\lambda(\mathbf{f}) = \frac{1}{2\sigma_{obj}^2}\mathbf{f}^t\left((\mathbf{I} + \mathbf{S}_0)^{-1} - (\mathbf{I} + \mathbf{S}_1)^{-1}\right)\mathbf{f}$$
$$\simeq \frac{1}{2\sigma_{obj}^2}\mathbf{f}^t(\mathbf{I} + \mathbf{S}_a)^{-1}\Delta\mathbf{S}\,(\mathbf{I} + \mathbf{S}_a)^{-1}\mathbf{f}\,. \tag{13}$$

Equation (13) equates the role of $(\mathbf{I} + \mathbf{S}_a)^{-1}\mathbf{f}$ to $\sigma_{obj}\Omega_a^{-1}\mathbf{H}^t\mathbf{g}$ in (12). Thus, the suggested beamformer is given by

$$\mathbf{g}_B = \mathbf{B}_{IW}^t \mathbf{g} \text{ where } \mathbf{B}_{IW}^t \triangleq \sigma_{obj}(\mathbf{I} + \mathbf{S}_a)\Omega_a^{-1}\mathbf{H}^t. \quad (14)$$

The major difference of $\mathbf{B}_{IW}^t$ from the WF bemformer $\mathbf{B}_{WF}^t$ in (7) is between the Ω_a and Ω_s matrices. Under the circulant assumption for each of the block Toeplitz matrices that assemble $\mathbf{H}$, Ω_s can be inverted by using a Discrete Fourier Transform (DFT) technique. The matrix Ω_a, however, includes an additional nonstationary term $\sigma_{obj}^2\mathbf{H}^t\mathbf{H}\mathbf{S}_a$, thus, cannot be inverted easily. For $\sigma_{obj}\Omega_a^{-1}\mathbf{H}^t\mathbf{g}$ to be calculated, we use another power series expansion by re-writing Ω_a^{-1} as

$$\Omega_a^{-1} = \Omega_s^{-1/2}(\mathbf{I} + \Omega_s^{-1/2}\sigma_{obj}^2\mathbf{H}^t\mathbf{H}\mathbf{S}_a\Omega_s^{-1/2})^{-1}\Omega_s^{-1/2}. \quad (15)$$

Applying the expansion to the term in parentheses, we have

$$\begin{aligned}
&\sigma_{obj}\Omega_a^{-1}\mathbf{H}^t\mathbf{g} \\
&= \sigma_{obj}\Omega_s^{-1/2}\left(\sum_{k=0}^{\infty}\left(-\sigma_{obj}^2\Omega_s^{-1/2}\mathbf{H}^t\mathbf{H}\mathbf{S}_a\Omega_s^{-1/2}\right)^k\right) \\
&\quad \times \Omega_s^{-1/2}\mathbf{H}^t\mathbf{g} \\
&= \left(\sum_{k=0}^{\infty}\left(-\sigma_{obj}^2\Omega_s^{-1}\mathbf{H}^t\mathbf{H}\mathbf{S}_a\right)^k\right)\sigma_{obj}\Omega_s^{-1}\mathbf{H}^t\mathbf{g}. \quad (16)
\end{aligned}$$

Equation (16) yields the iterative formula for calculating $\sigma_{obj}\Omega_a^{-1}\mathbf{H}^t\mathbf{g}$:

$$\begin{aligned}
&\mathbf{q}_{j+1} = -\sigma_{obj}^2\Omega_s^{-1}\mathbf{H}^t\mathbf{H}\mathbf{S}_a\mathbf{q}_j \quad \text{and} \\
&\mathbf{p}_{j+1} = \mathbf{p}_j + \mathbf{q}_{j+1}, \quad (17)
\end{aligned}$$

which is initialized with $\mathbf{q}_0 = \mathbf{p}_0 = \sigma_{obj}\Omega_s^{-1}\mathbf{H}^t\mathbf{g}$.

The iteration in (17) begins with the WF beamformed data, then adds higher-order terms of $\mathbf{S}_a$ until the calculation converges. We name $\mathbf{B}_{IW}^t$ the *Iterative Wiener* (IW) beamformer. It combines the WF beamformer with an iterative process for tuning the image based on the average variance map, $\mathbf{S}_a$. For a low-contrast task $\mathbf{S}_a \simeq \mathbf{S}_i \simeq \mathbf{0}$ so the iterations do not add much information to the generated image and the IW reduces to the WF beamformer.

The IW beamformer is similar to the *iterative Wiener filter* we developed for DS beamformed RF data.[15] This was a combination of the Wiener filter[19] with an iterative process that tuned the contrast inside the breast lesion. For the beamformer in the present paper, a major difference is that the data processing is extended to the transducer elements. Echo signals from individual channels are combined using a Matched filter before being further processed. The derivation of the Matched filter in the task-based framework was presented in our previous studies.[12,20] Another advance in this paper is the implementation of the beamformer on experimental data, in Sec. IV, where the underlying system is not known precisely.

III. OBSERVER STUDY

A. Observer efficiency

We evaluate and compare the IW to other beamformers using a panel of five tasks, described in Paper I. The tasks represent five typical BIRADS features in breast cancer diagnosis. We recall that Task 1 involves low-contrast detection while Tasks 2–5 are require high-contrast discrimination. Specifically, Task 2 relates to discrimination of an elongated eccentric lesion from a circular lesion; Task 3 is about discrimination of a soft, poorly defined boundary from a well-circumscribed boundary; Task 4 requires discrimination of a spiculated boundary from a circular boundary; and Task 5 involves discriminating a very weakly scattering hypoechoic interior from an anechoic (cyst-like) lesion interior.

Beamformer performance is assessed through a combination of the IO and Smith-Wagner (SW) observer over the five tasks. The SW observer was developed by Smith and Wagner[4,5] with the test statistic

$$\lambda_{SW}(\mathbf{b}) = \mathbf{b}^t\Delta\mathbf{S}\,\mathbf{b}. \quad (18)$$

This observer can be used to approximate the ideal observer applied to B-mode images for detecting low-contrast lesions (Task 1). In our study, we use it to approximate the ideal observer for the other four tasks as well. The observer performance ranges from 0.5 to 1. The difficulty of the task is controlled through the object contrast factor given by

$$C = \sum_j |[\Delta\mathbf{S}]_{jj}|, \quad (19)$$

where $\Delta\mathbf{S}$ is the task contrast. The observer efficiency is calculated using[12]

$$\eta = (C_I/C_{SW})^2, \quad (20)$$

where C_I and C_{SW} are the contrast factors for the IO and SW observers to achieve $P_c \simeq 0.8$. As the IO performance is a measure of task-relevant information, the efficiency quantifies the information loss during the transformation from the pre-beamformed data $\mathbf{g}$ to the B-mode image $\mathbf{b}$.

B. Data generation and beamformer computation

Under the LSI assumption, the pre-beamformed data are generated from convolutions between the scattering object and the pulse-echo impulse response for each channel, i.e., the element point-spread-function (psf). These functions are simulated by using Field II[21,22] with parameters extracted from the ULA-OP ultrasound system.[10] This device uses a linear array of 192 elements, each with dimensions 0.215 mm × 6.0 mm, separated by a 0.03 mm kerf. There are 64 elements active in each transmit and receive cycle. A 20-mm transmit/receive focal length was used. In elevation, the aperture is weakly-focused using an acoustic lens with a focal length of 20 mm. A three-cycle excitation voltage is applied to generate an ultrasound pulse with center frequency at 6.0 MHz and a 40% pulse-echo bandwidth. The RF echo signals were sampled at 50 Msamples/s, resulting in an axial sampling interval of 0.0154 mm. In the lateral direction the beam is stepped by a lateral spacing of 0.049 mm. The noise variance σ_n^2 was adjusted so that the echo SNR for

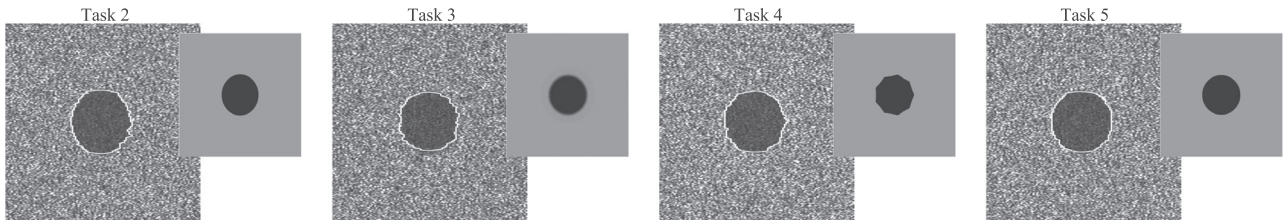

FIG. 1. Illustrations of the segmentation for Tasks 2–5 (high-contrast tasks). The segmentation is performed on Wiener-filtered B-mode (WF B-mode) images. The segmented results are shown with the corresponding variance maps for reference.

the DS beamformed RF signals is 24 dB. This is matched to the echo SNR calibrated at the focal depth of the ULA-OP system. The point-spread-functions are generated by scanning a point-scatterer at the focal depth of 20 mm.

The MV is implemented with the reduced-rank approximation of $\mathbf{H}^t\mathbf{H}$ to avoid ill-conditioning. We normalize the eigenvalues of $\mathbf{H}^t\mathbf{H}$ to the largest value and retain those above the level of −38 dB.[12] The WF beamformer can be calculated with the full-size $\mathbf{H}^t\mathbf{H}$ because of its natural regularization. To generate the IW image, the iterative process requires that either $\mathbf{S}_a$ is known or can be estimated from the data. Recall that $\mathbf{S}_i$ is a variance map defining the spatial extent of a diagnostic lesion feature and $\mathbf{S}_a$ is the average template for the benign and malignant features of a given task.

To be practical, we estimated $\mathbf{S}_i$ from the generated data by using a segmentation based on a Markov random field (MRF) model of the envelope image described previously.[15] The assumption is that each $\mathbf{S}_i$ has only two values corresponding to inside and outside the lesion area. The algorithm was originally developed for segmenting standard B-mode images.[23] In our study, we found that the best segmentation results were obtained by analyzing B-mode images produced by the Wiener filtered beamformer. Figure 1 illustrates the segmentation of the high-contrast cases (malignant class) in Tasks 2–5. The variance map used to generate the image is also shown in each sub-figure for reference.

Examples of envelope image pairs generated by each of the beamformers for Task 5 are shown in Fig. 2. The beamformers are applied to the same set of simulated data. In the figure, the image pair obtained by the IW beamformer offers the best discrimination between the contrasts insides the two lesions.

C. Numerical results

Figure 3 displays the observer efficiencies of the beamformers for discriminating malignant from benign features in Tasks 1–5. The DS has the lowest efficiency in all tasks. Both the WF and MV beamformers help to increase the efficiency in all the tasks. Compared to DS, the WF offers more than a fivefold improvement in Tasks 1–4. However, in Task 5, the increment is only about a factor of two (13.79% versus 7.21%). This is because the WF derivation is based on a low-contrast approximation. In this task, the MV has higher performance (15.61% versus 13.79%). However, that improvement comes from the reduced-rank approximation during the MV implementation.[12]

The IW beamformer, which is the WF beamformer combined with an iterative process, offers an efficiency in Task 5 of 35.80%, a fivefold improvement compared to the DS. This iterative approach also helps to increase the efficiency in the other tasks (Tasks 2–4), even if there are errors in the corresponding segmentations. The IW performance is limited primarily by these errors and the computation time. A brief discussion of the computational complexity for each beamformer is provided in Sec. V.

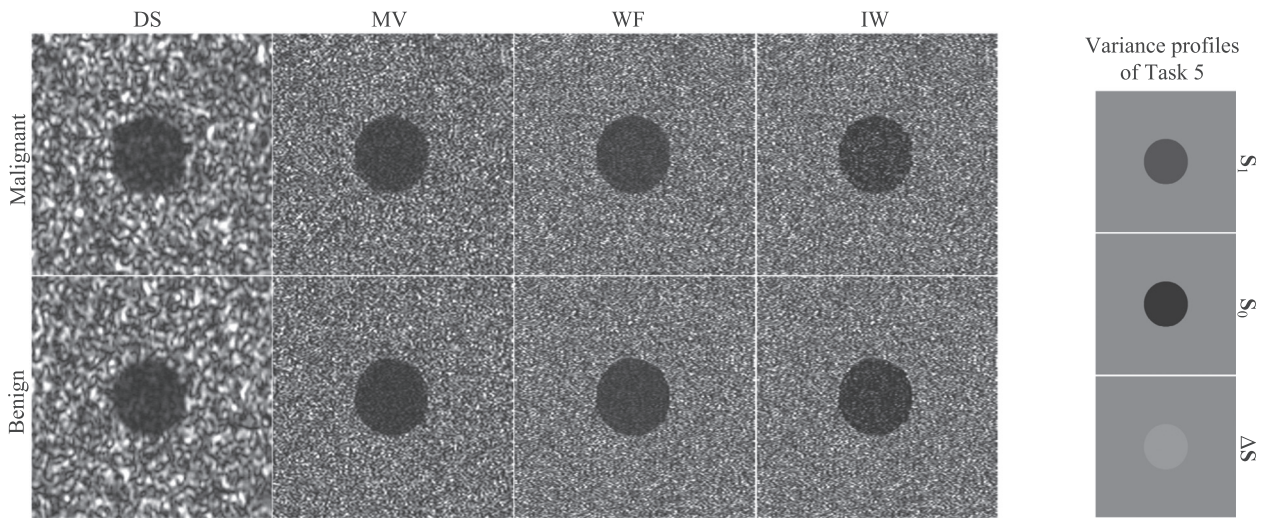

FIG. 2. Examples of image pairs (linear scale) for Task 5 [hypoechoic (top row) versus anechoic (bottom row)] using the same receive-channel echo data after applying beamformers in various combinations. DS is delay and sum; MV is the minimum variance; WF is the Wiener-filter; and IW is the Iterative Wiener. The variance profiles of Task 5 are on the right of the figure.

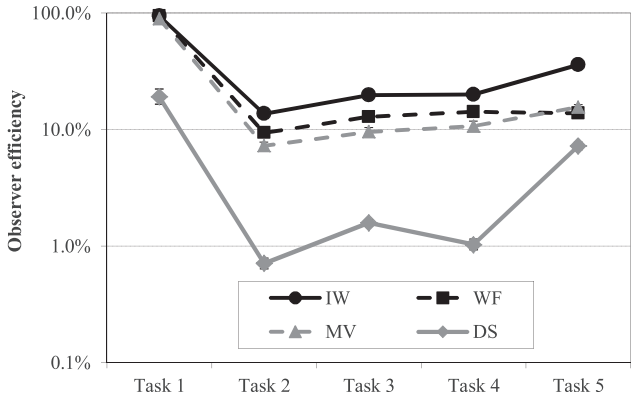

FIG. 3. Observer efficiencies measured for the beamformers illustrated Fig. 2 are plotted (log-scale) for the five discrimination tasks.

IV. EXPERIMENTAL IMPLEMENTATION

In this section, we apply the beamformers to echo data acquired from the ULA-OP system by scanning a tissue-mimicking phantom. The system parameters were nominally the same as those used in the simulation, described in Sec. III B.

A. Shift-invariant approximation

Conventional dynamic focusing is still the most popular method used to perform the spatiotemporal mapping and generate 2-D RF data. It reconstructs the frame line-by-line. One line is reconstructed at the center of the beam for each each transmit-receive sequence. The resulting RF data are the output of a linear shift-variant process.[24] The psfs that we use to characterize the data generation are only constant within small depth ranges. Thus, applying the derived beamformers to data generated with conventional dynamic focusing results in sub-optimal performance because of the LSI assumption. To implement our beamformers with a more accurate model, the image region can be divided into small patches. Beamforming is performed locally with the element psfs updated for each patch. This scheme was used in our work to apply the Wiener filter to the dynamic focused data.[25] It should be noted that the computation required to implement this increases significantly when it is extended to individual transducer elements.

Recently, we have developed pixel-based beamforming algorithms to improve ultrasound image resolution. The method generates the 2-D RF data frame pixel-by-pixel and data are collected from the received waveforms by using a *coherent time delay*. The generated B-mode images have an average speckle sizes in the near- and far-field as good as that at the focal depth.[16,17] In this study, we employ this coherent time delay to form 2-D RF data frames at each received channel before applying the beamformers. This allows us to construct beamformers with a single transmit focus configuration that have uniform point-spread-functions across the whole image.

For a comprehensive evaluation, we compare these beamformers to the delay-and-sum approach based on the coherent time delay. We name this method the coherent pixel-based delay-and-sum (CPB-DS) beamformer to differentiate it from conventional dynamic focusing. The CPB-DS beamformer and coherent time delay calculation are briefly summarized in the Appendix. Similar to our previous studies,[25,26] we construct the beamformers by using the psfs simulated with Field II program. Errors between the actual and simulated psfs, as well as those caused by the assumption of the circulant matrices, are treated as measurement noise of the system.

B. Evaluation metrics

We evaluate the beamformers through the quality of the generated images, measured using spatial resolution and contrast ratio.[27] The spatial resolution can be calculated from the width of the response to a single scatterer or by using the average size of speckle spots in the B-mode image, given by[4,5]

$$S_{\mathbf{x}} = \int_{-\infty}^{\infty} \frac{C_X(\mathbf{x})}{C_X(0)} d\mathbf{x}, \tag{21}$$

where $C_X(\mathbf{x})$ is the spatial auto covariance function (ACF) for the RF data, $d\mathbf{x}$ is the sampling interval 2-D vector, and $\mathbf{x} = (z, x)$. For each generated image, we calculate the coherence lengths S_{cz} and S_{cx} in the axial and lateral directions, respectively.

The contrast ratio between a lesion and the background is quantified by[28]

$$\mathrm{CR} = \frac{I_{out} - I_{in}}{\sqrt{I_{out}^2 + I_{in}^2}}, \tag{22}$$

where I_{in} and I_{out} are the mean intensities (in decibels) measured inside and outside the lesion, respectively. The contrast ratio (CR) has a value of 1 for perfect contrast, and a value of 0 for no contrast between the lesion and background. The background kernel is selected to have the same area as the lesion. To minimise the effect of variations in the attenuation and diffraction of the ultrasound, we choose the kernel as a circular ring enclosing the lesion.

C. Simulation study

We first apply the beamformers to data simulated by Field II that models the ULA-OP ultrasound system. We randomly place 30 000 equally strong point-scatterers in a 2-D imaging region of 12 mm × 31 mm (axis versus lateral directions). Those suspended inside a lesion have their amplitudes suppressed by 90%. The lesion is a circle 5 mm in diameter, located at a depth of 20 mm. The numerical phantom also has six highly scattering points distributed at three depths of 17.5, 20, and 22.5 mm. There are two at each depth, 1 mm apart. The transmit beam is focused at 20 mm. Data are generated by superposing signals echoed back from the scatterers, thus, it includes the shift-variant nature of the system. The MV beamformer is calculated using a low-rank approximation where the threshold level is set at −22 dB, selected by maximizing the CR calculated on the MV beamformed B-mode. The WF beamformer is calculated with a noise level set at 5% of the peak amplitude of the data. These

parameters are selected manually based on visualization of the generated images. When implementing the IW algorithm, only one image of the object is available (either benign or malignant), so we use $\mathbf{S}_i$ as approximation for $\mathbf{S}_a$. Therefore, to estimate the variance profile, $\mathbf{S}_a$, we apply a segmentation algorithm to the corresponding WF B-mode image and then measure the statistics of the two resulting regions.

Imaging results generated with beamformers are shown in Figs. 4(a)–4(d). The CPB-DS is displayed in image (a), while those with the MV, WF and IW beamformers are in Fig. 4(b)–4(d), respectively. Compared to the CPB-DS, the MV and WF B-mode images have higher spatial resolutions. However, the MV beamformed image has much lower contrast than that generated with the CPB-DS beamformer. The lesion contrast only shows substantial improvements with the IW beamformer. For detail comparison, we plot in Fig. 5 sections crossing through the pairs of scatterers in both lateral and axial directions. At each depth, we measure the full widths at half maximum (FWHM) and summarize the average in Table I, along with the CR calculated on each image.

Compared to the MV B-mode image, the WF B-mode has similar spatial resolution in the lateral direction, but offers some improvements in the axial direction. The WF also has a CR on par with the CPB-DS B-mode image. Through the iterative process, the IW B-mode offers the best lesion contrast while maintaining the smallest FWHMs, drawing on the underlying WF algorithm. The iterative process accurately accounts for the different statistical properties inside and outside the lesion area.

D. Phantom study

We apply the beamformers to data acquired from the ULA-OP system by scanning a tissue-mimicking phantom (manufactured by the Department of Medical Physics, University of Wisconsin, Madison, WI). The manufacturer-reported speeds of sound ranging from 1538 to 1551 m/s and the attenuation coefficient slope is 0.2 dB $\text{cm}^{-1}\text{MHz}^{-1}$. The object contrast in the lesion versus background is −24 dB at 7 MHz. The phantom contains circular targets, 5 mm in diameter, positioned around a depth of 23.5 mm. The transmit beam is focused at 20 mm. The MV beamformer is calculated with a −21 dB threshold level for the low-rank approximation of $\mathbf{H}^t\mathbf{H}$, also selected by maximizing the lesion contrast on the MV B-mode image. The WF beamformer is implemented with a noise level set at 8% of the peak amplitude of the data. The envelope images with different beamformers are shown in Figs. 6(a)–6(d).

Similar to the simulation study, the images generated with MV and WF show improvements in spatial resolution over the CPB-DS, measured in term of average speckle size. A big difference from the simulation study is that the WF B-mode image has the CR much lower than that of the CPB-DS, indicating the reduced performance of the WF beamformer on experimental data. The IW still has the best performance in both spatial resolution and contrast ratio. However, the shape of the segmented lesion is quite poor compared to that in simulation. In the experiments, the phantom lesion has a soft boundary which violates the two-level assumption of the segmentation algorithm.

To assess the extent to which uniform spatial resolution has been achieved over the imaging region, we measure the average speckle size in the generated B-mode images at the focus and in the far-field regions. The focal region ranges from 17.5 to 22.5 mm, while the far-field ranges from 22.5 to 27.5 mm. The speckle size in the near-field is affected by the quadratic phase factor, so we do not calculate it on this region. The quadratic phase factor and its effects have already been discussed in previous work.[29,30] The calculated average speckle sizes and CRs are summarized in Table II.

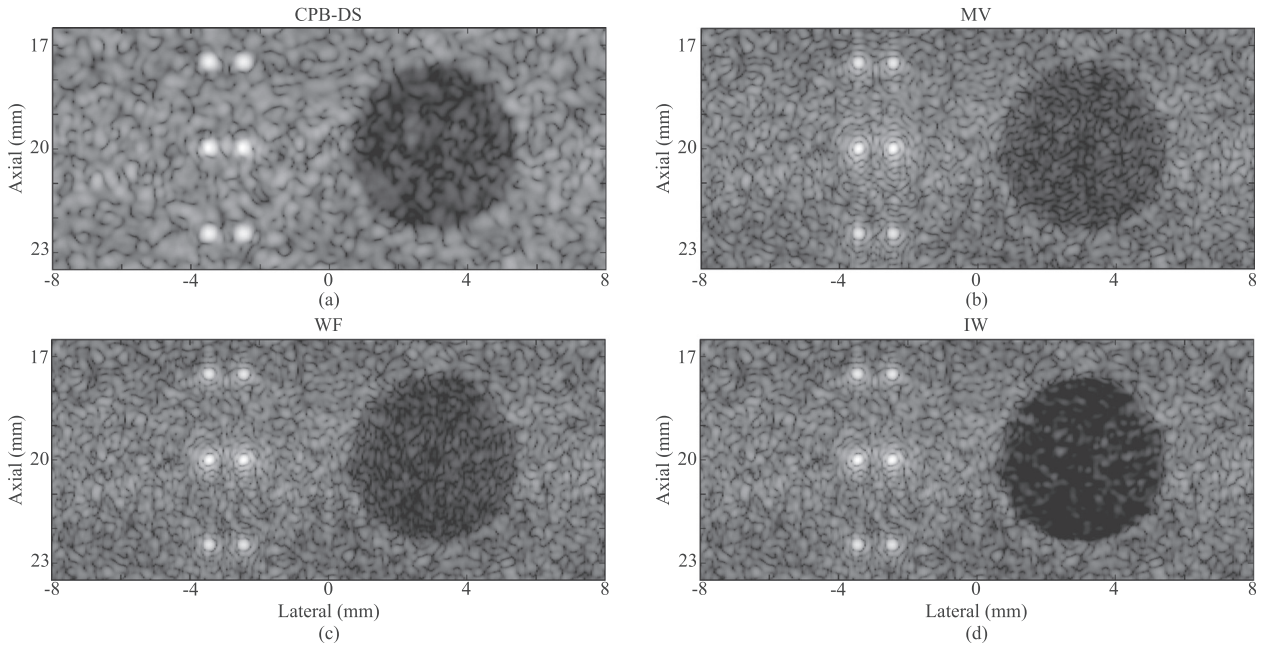

FIG. 4. Simulated images of a numerical phantom with six point-targets and an idealised lesion, 5 mm in diameter. The images are generated with different beamformers, including (a) CPB-DS, (b) MV, (c) WF, and (d) IW. The images are log-compressed and displayed with a dynamic range of 60 dB.

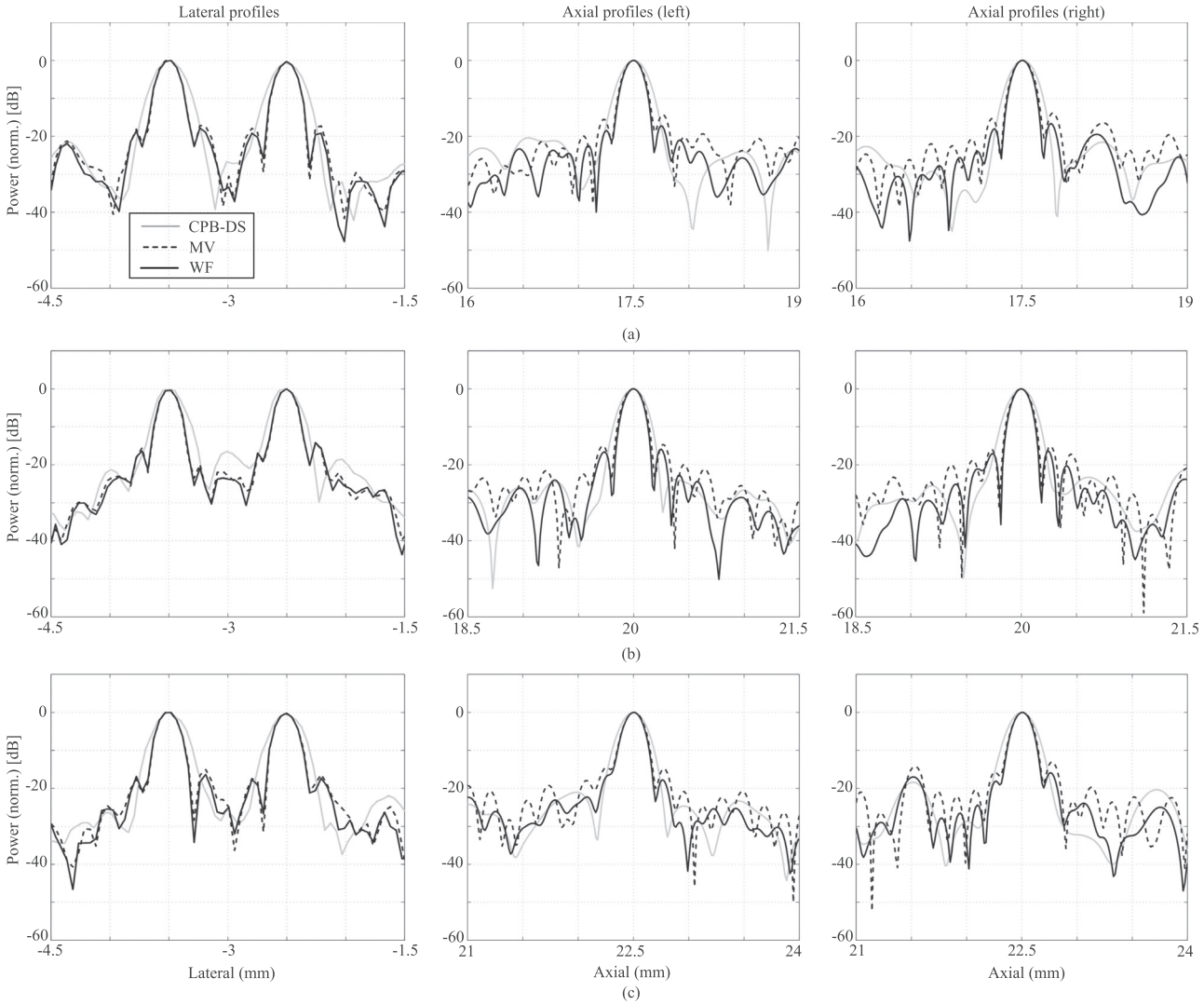

FIG. 5. The beam profiles for pairs of scatterers at depths of (a) 17.5 mm, (b) 20 mm, and (c) 22.5 mm. The graphs show the lateral response of the scatterers on the left, and two columns of axial responses on the right. The legend in the lateral response of (a) is also relevant to all the other plots. The beam profiles of the IW are the same as those of the WF beamformer, therefore, are not plotted in the figure.

V. DISCUSSION

In both the information-theoretical framework and the experiments, the IW beamformer is shown to have the best performance measured in terms of the image quality metrics. The high quality of the IW beamformed B-mode image comes from the combination of all the information available in the imaging context and backscattered signal. This includes detailed knowledge of the underlying system and task features, i.e., patient-specific information, to guide the decorrelation process. This requirement for task-specific information leads us to use image segmentation before the beamformer calculation. In the situation where the task information is known exactly, we find that the observer efficiency can reach 100%. Thus, segmentation errors are the main factor that limits the IW beamformer performance.

For fast computation, we implement a segmentation that is based on a two-level model. The resulting IW shows improvements on observer efficiencies across all discrimination tasks, but it offers the highest improvements in Task 5 where the efficiency is almost three times better than for the WF beamformer. This can be explained by the fact that any segmentation errors mainly affect the lesion edges, whereas the additional information obtained from the iterative process helps to determine the contrast inside the lesion which encodes the key feature of the task. The other tasks involving lesion edge discrimination would benefits more from the IW if we were to introduce a more efficient algorithm for segmentation.

TABLE I. FWHM and CR measured on the simulated images.[a]

	Average FWHM (in axial) at depth (mm)			Average FWHM (in lateral) at depth (mm)			
Beamformer	17.5	20	22.5	17.5	20	22.5	CR
CPB-DS	0.30	0.29	0.30	0.31	0.28	0.31	0.56
MV	0.23	0.23	0.23	0.22	0.21	0.23	0.48
WF	0.21	0.21	0.21	0.22	0.21	0.23	0.55
IW	0.21	0.21	0.21	0.22	0.21	0.23	0.81

[a]Wavelength $\lambda = c/f_0 = 0.257$ mm.

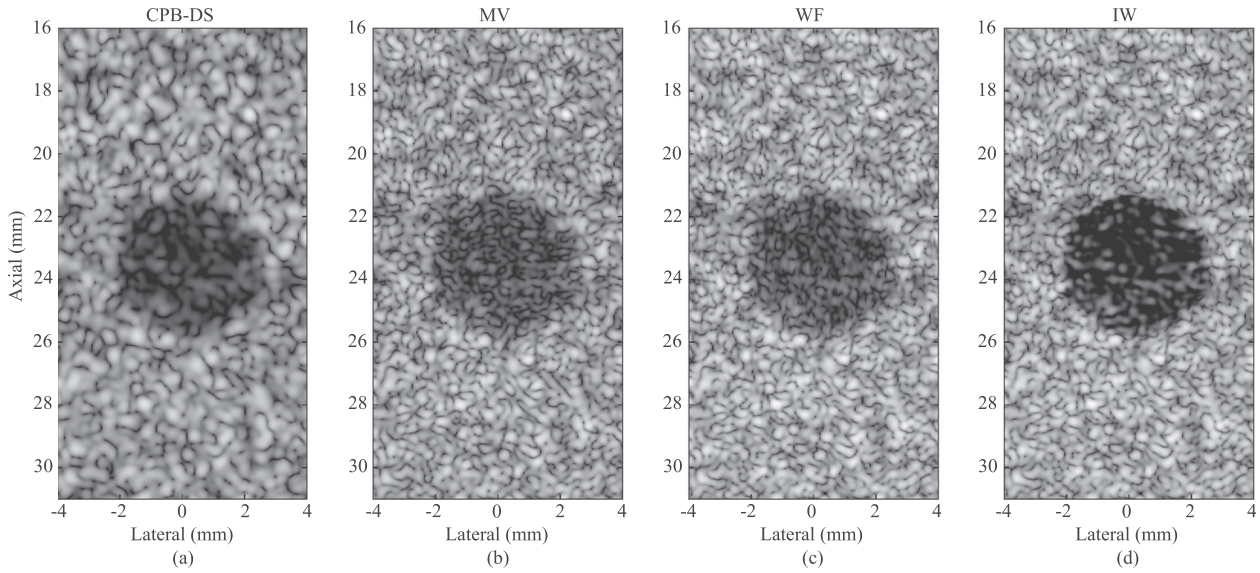

FIG. 6. Images of experimental data acquired with the ULA-OP system by imaging a lesion generated with different beamformers, including (a) CPB-DS, (b) MV, (c) WF, and (d) IW. The images are log-compressed and displayed with a dynamic range of 40 dB.

In experiments, we use the coherent time delay to generate the 2-D RF frame as the first step of implementing these beamformers. The imaging results, obtained with the CPB-DS method based on this time delay calculation, have similar speckle sizes across the imaging region. In effect, the resulting 2-D RF data frame can be viewed as the output of a LSI system. We can therefore proceed to design the beamformers based on this assumption. This allows for fast computation and a compact representation of the imaging system in the beamformer analysis.

Compared to the simulation study, improvements offered by the MV, WF, and IW in the experiments are reduced, especially in relation to the lesion contrast of the WF beamformed images. This comes from errors caused by a mismatch between the simulated and actual psfs of the system. The MV beamformed image has lesion contrast similar to that from the WF beamformer. This is explained by the low-rank approximation that is used when implementing the beamformer. It helps to reduce errors in modeling that affect the generated images. The experimental results could be improved if we were to measure the element psfs by calibration with hydrophones or using some sort of tomographic reconstruction algorithm.[31] Such methods are, however, beyond the scope of this paper.

TABLE II. Performance of beamformers on experimental data measured with image quality metrics.[a]

	Average speckle size on focal region		Average speckle size in far-field		
Beamformer	S_{cz} (mm)	S_{cx} (mm)	S_{cz} (mm)	S_{cx} (mm)	CR
CPB-DS	0.44 ± 0.020	0.43 ± 0.030	0.43 ± 0.010	0.45 ± 0.030	0.56
MV	0.32 ± 0.020	0.31 ± 0.010	0.30 ± 0.015	0.32 ± 0.020	0.46
WF	0.29 ± 0.015	0.29 ± 0.010	0.28 ± 0.010	0.31 ± 0.010	0.47
IW	0.29 ± 0.015	0.29 ± 0.010	0.28 ± 0.010	0.31 ± 0.010	0.67

[a]Azimuthal resolution $\lambda f^{\sharp} = 0.33$ mm.

Our beamformers are developed based on tasks in breast cancer diagnosis, hence, the temporal resolution or computational time is not a key metric in the evaluation of performance. Nevertheless, we briefly discuss the computational complexity of each beamformer. We take the active aperture to have size A ($A = 64$), the DS beamformer therefore involves $O(A)$ arithmetic operations. By using the circulant assumption for the transfer matrix, the WF and MV beamformers are calculated using (fast) Fourier transforms, which are applied to pre-summed RF data at each of the transducer elements. This involves a data vector with an M–dimension.[12] Thus, the computational complexity of WF and MV are both $O(AM \log(M))$. From Eq. (17), we see that the computation of the IW beamformer is given by $O(KAM \log(M))$, where K is the number of iterations. Yet, this still does not include the computation required for the segmentations. Computational analysis of the segmentation algorithm is beyond the scope of the present paper. In the Monte Carlo study, the IW requires up to 15.55 s, but most of the time is spent on the segmentation. Meanwhile, other beamformers require approximately 0.17 s for their calculations. The execution times are all measured using MATLAB (Mathworks Inc. Natick, MA) on a desktop PC (Windows 7, 64-bit system, Intel® Core™ i7-4770, and 8 Gb Memory).

VI. CONCLUSION

We have extended our task-based framework to develop the Iterative Wiener beamformer to improve the visual discrimination of BIRADS features, considered as critical signs in breast cancer diagnosis. The new beamformer is derived through an approximation of the ideal strategy that better adapts to high-contrast features of the scanned objects. As a result, the IW can maintain the high spatial resolution of the WF beamformer while preserving image contrast through an iterative process. Both numerical and experimental results show improvements from the IW beamformer over other

approaches, but at a cost of additional computation that is required for image segmentation.

We have also transformed the beamformers, derived in the theoretical framework, to practical implementations on an ultrasound open system by using the coherent time delay calculation. This allows us to calculate the beamformers with a convenient LSI approximation, which reduces the computational load. The experimental results show that the advanced beamformers achieve improvements over the DS method. Compared to the performance observed in simulation, however, we find the errors in system modeling can compromise the improvement offered by each beamformer. The greatest challenge when applying this framework in a clinical environment is to estimate accurately the imaging system impulse response functions. These functions are difficult to determine for many reasons such as phase aberrations, imperfection in transducer fabrication, and other system artefacts. When full information about these functions is available, the IO formalism enables us to design beamformers to make best use of it. Similarly, our approach enables the incorporation of prior patient-specific knowledge into the image processing to increase the diagnostic value of the resulting images.

The IW combination can be useful as prior information becomes increasingly important in breast cancer diagnosis. It may also support the emergence of multimodality systems in medical practice where prior information for ultrasound image processing is obtained from other modalities. We are striving to develop beamformers that are fast and robust across a wide spectrum of clinical features, and yet can adapt when necessary to special conditions. This statistical analysis provides a framework for that development.

ACKNOWLEDGMENT

The authors thank Dr. Craig Abbey of the University of California, Santa Barbara for advising and discussing many aspects of this work.

APPENDIX: CPB-DS

The CPB-DS beamformer uses the coherent time delay to collect data for individual imaging pixels. This time delay calculation was developed by using field pattern analysis. Details of the background and calculation are provided in recent papers.[16,17]

By analyzing the pressure field observed at each imaging point P, we found that the transmit wave-shape incident at the point can be described by two spherical pulses that correspond to the minimal and maximal distances from the point to the transmit aperture (assuming the sound-speed, c, is constant). This is a generalization of the time delay calculation in the virtual source element approach[32] that remains valid in regions where the virtual source approach is not applicable.

The two pulses have opposite phases and their magnitudes varying depending on the position of the imaging point. Figures 7(a) and 7(b) plot two different positions of point P versus the cross-sectional view of the transmit beam. By taking the delays at each transmit element into account, we model the aperture as an arc centered at the focus F with radius R_0. We also denote d as the focal depth, and R_1 and R_2 as distances from P to the edges of the arc. From F, we divide the imaging plane into four regions, denoted from (I) to (IV) clockwise, using the limited angle α from the virtual source approach.[33]

Let the arrival times of these pulses be $\tau^{tr}_{p,1}$ and $\tau^{tr}_{p,2}$. For P in region (I) [Fig. 7(a)], we have

$$\tau^{tr}_{p,1} = \frac{d-a}{c} \text{ and } \tau^{tr}_{p,2} = \frac{R_{\max}}{c} - \tau^{tr}_0, \tag{A1}$$

where $R_{\max} = \max(R_1, R_2)$. These results include a lag τ_0 which is the time between the activation of the first (outermost) and the last (center) elements, given by $\tau^{tr}_0 = (R_0 - d)/c$. In this region, the first pulse, $\tau^{tr}_{p,1}$, dominates the transmit wave-shape.

For P in region (III), the arrival times of these pulses are given by

$$\tau^{tr}_{p,1} = \frac{R_{\min}}{c} - \tau^{tr}_0 \text{ and } \tau^{tr}_{p,2} = \frac{d+a}{c}, \tag{A2}$$

where $R_{\max} = \min(R_1, R_2)$. In this region, the second pulse, $\tau^{tr}_{p,2}$, dominates the transmit wave-shape.

For P in region (II) [Fig. 7(b)], we have

$$\tau^{tr}_{p,1} = \frac{R_1}{c} - \tau^{tr}_0 \text{ and } \tau^{tr}_{p,2} = \frac{R_2}{c} - \tau^{tr}_0. \tag{A3}$$

The result is the same as for P in region (IV) except that now R_1 and R_2 are, respectively, the maximal and minimal distances from P to the arc. In regions (II) and (IV), the two pulses have similar magnitudes.

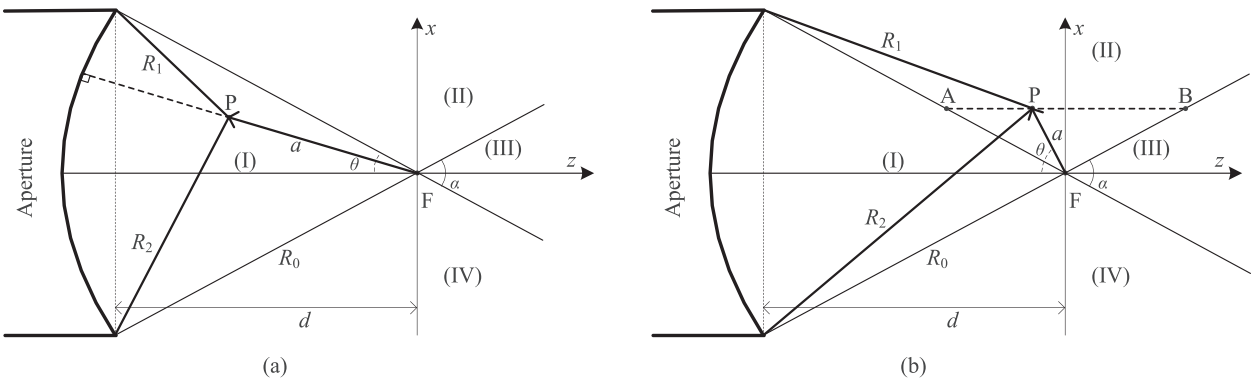

FIG. 7. The cross-sectional view of a focused beam used for the transmit time delay calculations.

On the basis of the arrival times of the two pulses, we extract two echo signals from the receive waveform, $r_{p,1}$ and $r_{p,2}$. These echos are combined linearly to generate data r_p for the CPB-DS beamformer, $r_p = a_1 r_{p,1} + a_2 r_{p,2}$. The coefficients (a_1, a_2) are selected as follows.

For P in region (I), $(a_1, a_2) = (1, 0)$ as the first pulse dominates the transmit wave-shape. For P in region (III), $(a_1, a_2) = (0, -1)$ as the second pulse dominates the wave-shape. This is similar to the strategy in the virtual source approach except for the minus sign associated with the data, $r_{p,2}$, from the second pulse. This minus sign is necessary in order to combine the two pulses with opposite phase that we found in our field pattern analysis. For P in region (II), we select (a_1, a_2) as

$$a_1 = \frac{|\mathbf{x}_b - \mathbf{x}_p|}{|\mathbf{x}_b - \mathbf{x}_a|} \text{ and } a_2 = -\frac{|\mathbf{x}_a - \mathbf{x}_p|}{|\mathbf{x}_a - \mathbf{x}_b|}, \tag{A4}$$

where $\mathbf{x}_a$, $\mathbf{x}_b$, and $\mathbf{x}_p$ are the position vectors of A, B, and P [see Fig. 7(b)]. Notice the minus sign for a_2, again, to account for the phase opposition between the two pulses.

The combined data r_p are superposed over all received channels and across all transmits to generate the CPB-DS beamformed data. In Secs. IV C and IV D, we show on both simulated and experimental data the CPB-DS generates a B-mode image that is artefact-free and has uniform speckle across the imaging region.

[1]R. F. Wagner and D. G. Brown, "Unified SNR analysis of medical imaging systems," Phys. Med. Biol. **30**(6), 489–518 (1985).
[2]N. Q. Nguyen, C. K. Abbey, and M. F. Insana, "Objective assessment of sonographic quality I: Task information," IEEE Trans. Med. Imag. **32**(4), 683–690 (2013).
[3]N. Q. Nguyen, C. K. Abbey, and M. F. Insana, "Objective assessment of sonographic quality II: Acquisition information spectrum," IEEE Trans. Med. Imag. **32**(4), 691–698 (2013).
[4]R. F. Wagner, S. W. Smith, J. M. Sandrik, and H. Lopez, "Statistics of speckle in ultrasound B-scans," IEEE Trans. Son. Ultrason. **30**(3), 156–163 (1983).
[5]S. W. Smith, R. F. Wagner, J. M. Sandrik, and H. Lopez, "Low contrast detectability and contrast/detail analysis in medical ultrasound," IEEE Trans. Son. Ultrason. **30**(3), 164–173 (1983).
[6]G. E. Trahey, J. W. Allison, S. W. Smith, and O. T. von Ramm, "A quantitative approach to speckle reduction via frequency compounding," Ultrason. Imaging **8**(3), 151–164 (1986).
[7]R. F. Wagner, M. F. Insana, and S. W. Smith, "Fundamental correlation lengths of coherent speckle in medical ultrasonic images," IEEE Trans. Ultrason. Ferroelectr. Freq. Control **35**(1), 34–44 (1988).
[8]J. M. Thijssen, B. J. Oosterveld, and R. F. Wagner, "Gray level transforms and lesion detectability in echographic images," Ultrason. Imaging **10**(3), 171–195 (1988).
[9]T. J. Hall, M. F. Insana, L. A. Harrison, N. M. Soller, and K. J. Schlehr, "Ultrasound contrast-detail analysis: A comparison of low-contrast detectability among scanhead designs," Med. Phys. **22**(7), 1117–1125 (1995).
[10]P. Tortoli, L. Bassi, A. Dallai, F. Guidi, and S. Ricci, "ULA-OP: An advanced open platform for ultrasound research," IEEE Trans. Ultrason. Ferroelec. Freq. Control **56**(10), 2207–2216 (2009).
[11]R. J. Zemp, C. K. Abbey, and M. F. Insana, "Linear system models for ultrasonic imaging: Application to signal statistics," IEEE Trans. Ultrason. Ferroelec. Freq. Control **50**(6), 642–654 (2003).
[12]N. Q. Nguyen, R. W. Prager, and M. F. Insana, "A task-based analytical framework for ultrasonic beamformer comparison," J. Acoust. Soc. Am. **140**(2), 1048–1059 (2016).
[13]G. H. Golub and C. F. Van Loan, *Matrix Computations*, 3rd ed. (Johns Hopkins University Press, Baltimore, MD, 1996), Chap. 2, pp. 48–96.
[14]M. A. Woodbury, "Inverting Modifies Matrices," Memo. Rep. 42 (Statistical Research Group, Princeton, NJ, 1950), 4 pp.
[15]N. Q. Nguyen, C. K. Abbey, and M. F. Insana, "An adaptive filter to approximate the Bayesian strategy for sonographic beamforming," IEEE Trans. Med. Imag. **30**(1), 28–37 (2011).
[16]N. Q. Nguyen and R. W. Prager, "High-resolution ultrasound imaging with unified pixel-based beamforming," IEEE Trans. Med. Imag. **35**(1), 98–108 (2016).
[17]N. Q. Nguyen and R. W. Prager, "Minimum variance approaches to ultrasound pixel-based beamforming," IEEE Trans. Med. Imag. **36**(2), 374–384 (2017).
[18]H. H. Barrett and K. J. Myers, *Foundations of Image Science* (John Wiley and Sons, Hoboken, NJ, 2004), Chap. 13, pp. 801–912.
[19]C. K. Abbey, R. J. Zemp, J. Liu, K. K. Lindfors, and M. F. Insana, "Observer efficiency in discrimination tasks simulating malignant and benign breast lesions with ultrasound," IEEE Trans. Med. Imag. **25**(2), 198–209 (2006).
[20]C. K. Abbey, N. Q. Nguyen, and M. F. Insana, "Optimal beamforming in ultrasound using the ideal observer," IEEE Trans. Ultrason. Ferroelectr. Freq. Control **57**(8), 1782–1796 (2010).
[21]J. A. Jensen and N. B. Svendsen, "Calculation of pressure fields from arbitrarily shaped, apodized, and excited ultrasound transducers," IEEE Trans. Ultrason. Ferroelec. Freq. Control **39**(2), 262–267 (1992).
[22]J. A. Jensen, "Field: A program for simulating ultrasound systems," Med. Biol. Eng. Comp. **34**(Suppl. 1), 351–353 (1996).
[23]E. A. Ashton and K. J. Parker, "Multiple resolution Bayesian segmentation of ultrasound images," Ultrasonic Imaging **17**(4), 291–304 (1995).
[24]J. Ng, R. Prager, N. Kingsbury, G. Treece, and A. Gee, "Modelling ultrasound imaging as a linear, shift-variant system," IEEE Trans. Ultrason. Ferroelectr. Freq. Control **53**(3), 549–563 (2006).
[25]H. Gomersall, D. Hodgson, R. Prager, N. Kingsbury, G. Treece, and A. Gee, "Efficient implementation of spatially-varying 3-D ultrasound deconvolution," IEEE Trans. Ultrason. Ferroelectr. Freq. Control **58**(1), 234–238 (2011).
[26]H.-C. Shin, R. Prager, H. Gomersall, N. Kingsbury, G. Treece, and A. Gee, "Estimation of average speed of sound using deconvolution of medical ultrasound data," Ultrasound Med. Biol. **36**(4), 623–636 (2010).
[27]C.-I. C. Nilsen and S. Holm, "Wiener beamforming and the coherence factor in ultrasound imaging," IEEE Trans. Ultrason. Ferroelectr. Freq. Control **57**(6), 1329–1346 (2010).
[28]S. Mehdizadeh, A. Austeng, T. F. Johansen, and S. Holm, "Eigenspace based minimum variance beamforming applied to ultrasound imaging of acoustically hard tissues," IEEE Trans. Med. Imag. **31**(10), 1912–1921 (2012).
[29]M. F. Insana, T. J. Hall, and L. T. Cook, "Backscatter coefficient estimation using array transducer," IEEE Trans. Ultrason. Ferroelec. Freq. Control **41**(5), 714–723 (1994).
[30]J. W. Goodman, *Introduction to Fourier Optics* (McGraw-Hill, New York, 1996), Chap. 4, pp. 63–96.
[31]N. Q. Nguyen, C. K. Abbey, R. D. Yapp, and M. F. Insana, "Tomographic reconstruction of the pulse-echo spatiotemporal impulse response," in *Proceedings of Society of Photo-Optical Instrumentation Engineers (SPIE)* (2010), Vol. 7629, pp. 1–11.
[32]R. Zemp and M. F. Insana, "Imaging with unfocused regions of focused ultrasound beams," J. Acoust. Soc. Am. **121**(3), 1491–1498 (2007).
[33]M. H. Bae and M. K. Jeong, "A study of synthetic-aperture imaging with virtual source elements in B-mode ultrasound imaging systems," IEEE Trans. Ultrason. Ferroelec. Freq. Control **47**(6), 1510–1519 (2000).